Available online at www.sciencedirect.com

ScienceDirect

journal homepage: www.elsevier.com/locate/he

New insights into the temperature-water transport-performance relationship in PEM fuel cells

Antonio Martín-Alcántara [a], *Javier Pino* [b], *Alfredo Iranzo* [a,b,*]

[a] *AICIA-Thermal Engineering Group, Camino de Los Descubrimientos, s/n, Sevilla, 410092, Spain*
[b] *Thermal Engineering Group, Energy Engineering Department, University of Seville, Camino de Los Descubrimientos, s/n, Sevilla, 410092, Spain*

HIGHLIGHTS

- Developed CFD model is validated with IV curve and local water distributions.
- Liquid water generation and transport is analyzed in a single channel straight fuel cell.
- Under-rib/under-channel water distributions are investigated.
- Novel scatter plots are created to explain existing relationships between water-related magnitudes.

GRAPHICAL ABSTRACT

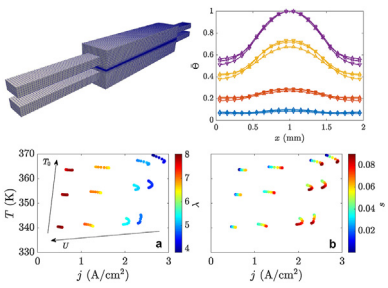

ARTICLE INFO

Article history:
Received 3 November 2022
Received in revised form
17 December 2022
Accepted 23 December 2022
Available online 10 January 2023

Keywords:
PEMFC
Fuel cell
Single straight-channel
Water management
CFD
Numerical model

ABSTRACT

Three-dimensional numerical simulations of a single straight-channel PEMFC at three different operating temperatures (343 K, 353 K, and 363 K) and at a relative humidity $RH = 90\%$ were carried out, by using potentiostatic conditions ranging from 0.27 to 1.0 V. This study aimed at gaining further insights into the complex and tightly coupled interactions taking place inside the fuel cell, relating water generation and transport with local temperature distributions and cell performance. A sensitivity analysis concluded that the higher the operating temperature is, the better the electrical performance of the PEMFC, for the range of operating temperatures analyzed. This feature was further investigated at high current densities ($j = 2.25$ and 2.57 A/cm^2), where the increase of the operating temperature (in the range of study) resulted in an enhancement of the water diffusivity and the electro-osmotic drag, improving the ionic conductivity. Additionally, the dimensionless temperature distribution across the cell width was found to be similar in all the cases. Profile-like curves displaying under-rib/under-channel characteristics are presented and analyzed to understand the role of water and its interaction with the different phenomena occurring within the cell. It was demonstrated that colored scatter plots are convenient tools that contribute to explain existing relationships between the water-related magnitudes.

* *Corresponding author*. AICIA-Thermal Engineering Group, Camino de los Descubrimientos, s/n, Sevilla, 410092, Spain.
E-mail address: airanzo@us.es (A. Iranzo).

https://doi.org/10.1016/j.ijhydene.2022.12.281

Introduction

Proton-Exchange Membrane Fuel Cells (PEMFCs), directly converting fuel into electric energy through a solid electrolyte membrane, have become one of the most promising devices in the last few years for the electrical conversion of stored H_2, the automotive sector being one of the key applications, which represents a significant contribution to total global emissions worldwide [1]. Without a thermodynamic cycle or mobile parts reducing the lifespan of the equipment, fuel cells have become promising candidates for the energy transition in the forthcoming years [2]. Nevertheless, some recent hydrogen-fueled applications such as micro planar combustors [3] combined with thermophotovoltaic devices have received great interest because they also represent efficient alternatives to e.g. conventional batteries. Back to the PEM fuel cells, the electrochemical reactions taking place inside the cell (oxidation and reduction) are simple and occur simultaneously on both sides of the electrolyte. Basically, the anode is fed with hydrogen and the cathode with oxygen (or air), generating an electric potential in between the fuel cell terminals. Involved in the process there also exist other components such as the Gas Diffusion Layers (GDLs), improving the diffusion of the species perpendicular to the flow direction (through-plane), and the Catalyst Layers (CLs), containing platinum or platinum alloys (typically Pt/C), where the reaction actually takes place. The membrane, with a typical operating temperature around 40–90 °C, represents the core of the PEMFC, permitting the pass of protons but not the electrical current. All the components are engineered in between highly conductive plates that eventually transport the electrical power. Thus, the overall reaction in the PEMFC can be regarded as an exothermic process derived from the H_2 electro-oxidation that generates not only electricity, but heat and water as outputs [4], both of them influencing the fuel cell performance. For instance, membrane may suffer from overheating, reducing its hydration (and the cell performance consequently) and the lifespan of the components. At high operating current densities, the water generation becomes important because porous layers can be invaded (flooding effect), compromising the diffusion of the species, which naturally results in a poorer PEMFC performance [5,6].

Thus, water and heat management remains a major obstacle to the successful commercialization of proton exchange membrane fuel cells, as pointed out by Ijaodola et al. [7]. For instance, Pourrahmani et al. [8] recently delivered a comprehensive review on the key operational challenges and solutions to improve water/thermal management from both experimental, analytical, and numerical viewpoints. In addition to presenting the fundamental theory for an analytical model development, the impacts of microstructural properties and the design of the porous layers on the water/thermal management are described. Yang et al. [9], on the other hand, studied a transient PEMFC system model, including a 40-fuel-cells stack, membrane humidifier, electrochemical hydrogen pump, air compressor, and radiator, analyzing the impact of some operating conditions such as the air stoichiometry or the current density on the fuel cell performance. The results show that under low operating current densities, increasing the operating temperature of membrane humidifier is unfavorable as it intensifies the membrane dehydration, but if the temperature of dry air flowing into humidifier is well managed the membrane dehydration may be avoided, and assisted heating methods for humidifier may be unnecessary. As an alternative to deal with water management, different configuration of bioinspired models (see Ref. [10] for a detailed review) were experimental and numerically tested in Ref. [11], but only a 6.0%-higher power peak was obtained (in the best of cases) with respect to the reference design.

To prevent these issues, it is necessary to be able to predict the performance of potential fuel cell designs prior to manufacturing, so that numerical simulations have become an essential tool saving important costs and time in this process. Otherwise, the assembly of several PEMFC prototypes, the experimental campaigns and the final post-processing would result in a highly impractical sequence. Indeed, the measurement of certain variables during the PEMFC operation is not always possible (or economically affordable) because fuel cells are compactly closed devices with components of very small scales, requiring very sophisticated techniques for this purpose. For example, neutron radiography can be useful for the estimation of the water content inside the cell, as e.g. performed in Refs. [12,13]. A recent technique for the measurement of through-plane diffusivity was developed in Ref. [14].

Consequently, this work emphasizes the capabilities of numerical simulations, and it is aimed at the study of the performance of a single straight-channel 3D fuel cell, by inspecting the behavior of most relevant variables under-rib and under-channel, as well as their interactions with water. For ease of analysis, averaging in the longitudinal direction was carried out, but more interesting are the colored scatter plots interrelating water magnitudes against temperature and current density for the different operating conditions. Such novel analysis provides a more comprehensive method to understand the relationship appearing between the mentioned variables. A work of interest studying numerically the water transport mechanism inside a single straight-channel PEMFC (comparable to that of this study) is that of [15]. The spatial (longitudinal) evolution of the water mass fraction is exclusively analyzed at 353 K for a different range of voltages, concluding with the different relationships observed in successive simulations. A similar three-dimensional numerical work in Ref. [16] analyzes the gradient porosity distribution in the cathode GDL to enhance the mass transfer and

water removal of a PEMFC. Also of interest is the numerical work [17] in which several GDLs with and without MPL are compared. Alternatively, the different configurations of serpentine flow in channels enhancing the fuel cell performance are evaluated numerically in Ref. [18]. Su et al. [19] also conducted CFD simulations for the prediction of the performance of a high-temperature PEMFC, given a three-dimensional model, and concluding that the higher the inlet temperature, system pressure or flow rate, the better the performance. However, the internal physical processes enhancing the performance were not studied in detail. A novel design inspired serpentine and parallel flow channels called V-Ribbed is explored in Ref. [20] through CFD simulations. A superior performance of the PEMFC has been observed, increasing the mass transfer, and improving the water management and so on the cell performance. Alternatively [21], used 3D numerical simulations to explore straight parallel, wavy consistent and wavy interdigitated channels configurations at 353 K, concluding that wavy-like patterns (consistent or not) enhance the performance of the fuel cell due to the uniform gas distribution.

The content of this paper is as follows. First, the formulation of the model and the numerical settings are described in section 3.2. Next, in section 3 the results corresponding to the different operating temperatures are compared and discussed. The interaction between the water-related magnitudes, current density and temperature are discussed via colored scatter plots, which provides a compact way to correlate the interactions taking place between different magnitudes. Finally, some conclusions and future research directions are provided in section 4. For readability, a thorough grid sensitivity study and model validation can be found in Supplementary Material. Additional contour plots compositions for each case in study are also provided in that section.

Problem description and numerical model

Conservation equations for species, momentum, energy, liquid water volume fraction, membrane phase and solid phase potentials are solved in the three-dimensional PEMFC model of Fig. 1(*a*) by adopting the Finite Volume Method (FVM) and the existing add-on module in ANSYS Fluent v18.0 [22,23]. Several authors [24–28] also succeeded in reproducing PEMFC characteristics with this software.

The geometry of the single straight-channel of aspect ratio Rib/Channel = 1.0/1.0 mm was reproduced numerically from the experiments of Tabuchi et al. [12] (see Table 1) only considering a single straight channel, and from the

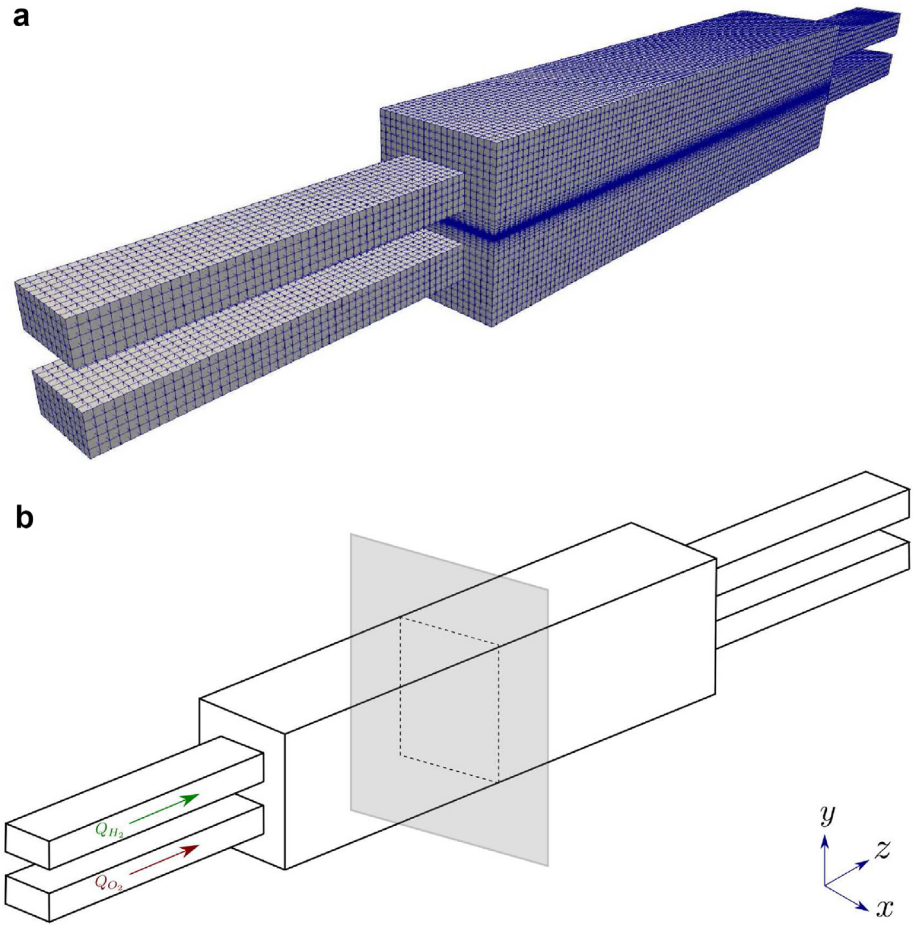

Fig. 1 – (*a*) External view of the Mesh #1 (see Supplementary Material), (*b*) schematic of the single straight-channel PEMFC and the XY– plane (or z– direction) over which the magnitudes were averaged.

Table 1 – MEA specification and operating condition (from Tabuchi et al. [12]).

Experimental data	
Membrane thickness (μm)	30.0
Catalyst layer	Pt/C, 0.4 mg/cm^2 Pt loading at both sides
GDL	Carbon paper
CL thickness (mm)	0.01
Active area (cm^{-2})	1.0
Flow field	Straight channel
Porosity of CL	0.5
Cell temperature (K)	353 K
Relative humidity, RH (%)	$RH_a/RH_c = 90/90$
Inlet pressure, P (kPa)	250
Stoichiometry	Large stoichiometry (2.0 L/min)

simulations of Corda et al. [29]. Some characteristic properties are summarized in Table 2.

Regarding the reliability of the results, an in deep validation and verification study was conducted, concluding that both the grid density and the domain size were sufficient to accurately model the processes taking place during the PEMFC performance. The grid sensitivity analysis in fig. S1 analyzes the averaged liquid water saturation across GDLs at three different grid density levels and $U = 0.65$ V. The results in fig. S2 supports the validity of the model compared to the experiments from Ref. [12]. Further information can be found in Supplementary Material.

For the numerical discretization, second-order schemes were selected for the entire range of variables of the problem, namely: pressure, density, momentum, species, energy, electric potential, capillary pressure, water content, and liquid saturation in channels. The boundary conditions are set similarly to Ref. [29]. Symmetry conditions were fixed at the PEMFC sides. A volumetric flux of H_2 and O_2 corresponding to the 2 L/min at $RH = 90\%$ introduced experimentally in Ref. [12] was prescribed both at anode and cathode. Outflow boundary conditions (i.e., $\partial\mathbf{V}/\partial\mathbf{n} = 0$ and $p = 0$, with $\mathbf{V}$ and p the velocity vector and the pressure relative to the operating, respectively) at the outlet were applied. For the rest of the walls the nonslip condition was adopted. The temperature on the terminal plates and inlet gases was fixed to the corresponding $T_0 = 343$ K, 353 K or 363 K, and adiabatic elsewhere. The operating pressure was of 250 kPa. Although potentiostatic boundary conditions ranging from 0.27 to 1.0 V (see Fig. 2) were adopted, additional simulations at fixed $j = 2.25$ and 2.57 A/cm^2 were conducted for illustration of some of the results.

Table 2 – Physical and transport properties (from Corda et al. [29] and Iranzo et al. [24] if not available from Tabuchi et al. [12]).

Geometric and physical properties	
Rib/channel width (mm)	1.0
Channel depth (mm)	0.5
GDL thickness (mm)	0.2
CL thickness (mm)	0.01
Membrane thickness (mm)	0.03
Porosity of GDL	0.7
Porosity of CL	0.5
GDL gas permeability (m^2 × 10^{-12})	4.0
CL gas permeability (m^2 × 10^{-13})	4.0
Surface-to-volume ratio (m^2/m^3 × 10^7)	5.0
Contact angle of GDL, θ_c (°)	110
Contact angle of CL, θ_c (°)	110
Surface tension between liquid water and air (N/m)	0.0625
Thermal conductivity of bipolar plate [W/(m K)]	20.0
Thermal conductivity of GDL [W/(m K)]	3.0
Thermal conductivity of CL [W/(m K)]	10.0
Thermal conductivity of membrane [W/(m K)]	0.95

In the following, the equations governing the physical and electrochemical processes involved in the PEMFC simulations are enumerated [22]. Other than these, the model formulation remain the same as that presented in Ref. [30]. Finally, conditions of steady state, laminar flow, ideal gases, isotropic porous media and constant operating temperatures are assumed by the PEMFC model.

- *Electrochemistry model:* The exchange current densities in anode and cathode have the following general definitions:

$$R_a = [\zeta_a j_a(T)]\left(\frac{[A]}{[A]_{ref}}\right)^{\gamma_a}\left(e^{\alpha_a^a F\eta_a/(RT)} - e^{-\alpha_c^a F\eta_a/(RT)}\right), \quad (1)$$

$$R_c = [\zeta_c j_c(T)]\left(\frac{[C]}{[C]_{ref}}\right)^{\gamma_c}\left(-e^{\alpha_a^c F\eta_c/(RT)} + e^{-\alpha_c^c F\eta_c/(RT)}\right), \quad (2)$$

where $j(T)$ is the exchange current density, ζ the specific active surface area, $[A|C]$ and $[A|C]_{ref}$ the respective local and reference species concentration, η is the surface overpotential, γ the concentration dependence, α_x^y the (dimensionless) charge transfer coefficients from the electrode x to the y, F the Faraday constant (9.65 × 10^7 C/kmol), R the universal gas constant, and T the temperature. The exchange current densities $j(T)$ depend on the local temperature in the form:

$$j_a(T) = j_a^{ref} e^{-E_a/(RT)\left(1-T/T_a^{ref}\right)}, \quad (3)$$

$$j_c(T) = j_c^{ref} e^{-E_c/(RT)\left(1-T/T_c^{ref}\right)}, \quad (4)$$

with E the reversal potential given by Nernst equation, and j^{ref} the reference exchange current density at the given temperature T^{ref}. It is worth mentioning that the open circuit

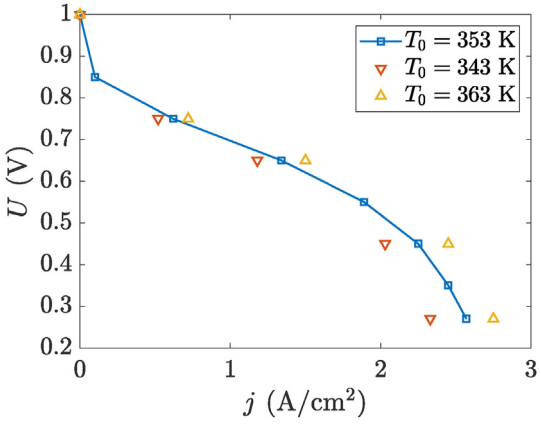

Fig. 2 – Polarization curves comparing the different operating temperatures in study.

voltage was fixed to 1.0 V as observed in the experiments of Tabuchi et al. [12].

- *Dissolved phase model:* The generation and transport of dissolved water is described by Ref. [31] as

$$\frac{\partial}{\partial t}\left(\epsilon_i M_{H_2O}\frac{\rho_i}{EW}\lambda\right)+\nabla\cdot\left(j_m\frac{n_d}{F}M_w\right)=\nabla\cdot\left(M_w D_w^i\nabla\lambda\right)+S_\lambda+S_{gd}+S_{ld}, \tag{5}$$

where M_{H_2O} is the molecular weight of water, ϵ is the porosity of the porous media, $j_m=-\sigma_{mem}\nabla\phi_{mem}$ is the ionic current density vector, λ is the dissolved water content, D_w^i the diffusion coefficient of water content, and S_λ, S_{gd} and S_{ld}, are the rates of water generation in CL, of mass change between gas/dissolved phases, and of liquid/dissolved phases, respectively. According to Ref. [32], the S_{gd} and S_{ld} rates are given by

$$S_{gd}=(1-s^\theta)\gamma_{gd}M_{H_2O}\frac{\rho_i}{EW}(\lambda_{eq}-\lambda), \tag{6}$$

$$S_{ld}=s^\theta\gamma_{ld}M_{H_2O}\frac{\rho_i}{EW}(\lambda_{eq}-\lambda), \tag{7}$$

with ρ_i the dry membrane density, EW its equivalent weight, s the liquid saturation level, λ_{eq} the equilibrium water content, γ_{gd} and γ_{ld} the gas and liquid mass exchange rate constants, and θ the exponent that is used to compute the phase-change rates (6) and (7).

The equilibrium water content is computed at the same time [32] as

$$\begin{aligned}\lambda eq=&\,0.3+6\,a\,[1-\tanh(a-0.5)]\\&+0.69\,(9.2-3.52)a^{1/2}\left[1+\tanh\left(\frac{a-0.89}{0.23}\right)\right]\\&+s\,(16.13-9.2),\end{aligned} \tag{8}$$

with

$$a=p_{wv}/p_{sat} \tag{9}$$

the water activity, and p_{wv} and p_{sat} the water vapor partial pressure and the saturation pressure, respectively.

- *Liquid phase model:* The transport equation for the liquid phase is driven by the pressure gradient ∇p_l following [32] as

$$\frac{\partial}{\partial t}(\epsilon_i\rho_l s)=\nabla\cdot\left(\frac{\rho_l K K_r}{\mu_l}\nabla p_l\right)+S_{gl}-S_{ld}, \tag{10}$$

where ρ_l is the liquid density, μ_l the liquid dynamic viscosity, K and K_r the absolute and relative permeability, and p_l the liquid pressure. The relative permeability is computed in the GDLs as

$$K_r=s^b, \tag{11}$$

where b is a given exponent, and in membrane

$$K_r=\left(\frac{\frac{M_{H_2O}}{\rho_l}\lambda_{s=1}+\frac{EW}{\rho_i}}{\frac{M_{H_2O}}{\rho_l}\lambda+\frac{EW}{\rho_i}}\frac{\lambda}{\lambda_{s=1}}\right)^2. \tag{12}$$

Because the liquid pressure can be expressed as the sum of the capillary p_c and gas pressure p, eq. (10) can be rewritten as

$$\frac{\partial}{\partial t}(\epsilon_i\rho_l s)=\nabla\cdot\left(\frac{\rho_l K K_r}{\mu_l}\nabla(p_c+p)\right)+S_{gl}-S_{ld}, \tag{13}$$

to be used where necessary. For the calculation of the capillary pressure, Leverett function is applied.

In addition, liquid water reduce the effective active surface are in CLs, so that the transfer currents are penalized by

$$R_j=(1-s)^{\gamma_j}R_j, \tag{14}$$

where γ_j is the exponent accounting for the liquid blockage to the reaction surface in Eqs. (1)–(4).

- Properties:
  - Gas phase species diffusivity:

thinsp; The dilute approximation method is used for this calculation, i.e.

$$D_i=\epsilon^{1.5}(1-s)^{r_s}D_i^0\left(\frac{p_0}{p}\right)^{\gamma_p}\left(\frac{T}{T_0}\right)^{\gamma_t}, \tag{15}$$

D_i^0 being the mass diffusivity of species i at the reference temperature and pressure (p_0, T_0) [33], and r_s the exponent of pore blockage. In general,

$$\begin{aligned}p_0&=101325\ \mathrm{N/m^2},\\T_0&=300\ \mathrm{K},\\\gamma_p&=1.0,\\\gamma_t&=1.5.\end{aligned}$$

$$D_w^i=\eta_\lambda\frac{\rho_i}{EW}f(\lambda), \tag{16}$$

where η_λ is a generic coefficient, and the function $f(\lambda)$ has been computed from Wu et al. [34] as

$$f(\lambda)=4.1e^{-10}\left(\frac{\lambda}{25}\right)^{0.15}\left[1+\tanh\left(\frac{\lambda-2.5}{1.4}\right)\right]. \tag{17}$$

$$n_d=\eta_{osm}\,g(\lambda), \tag{18}$$

with η_{osm} a generic factor. The function $g(\lambda)$ is given by

$$g(\lambda)=2.5\frac{\lambda}{22}. \tag{19}$$

For the sake of summary, the value of the parameters used in the simulations are given in Table 3. Although there exist sophisticated and accurate methods to fine-tune the model parameters (see e.g. Rezk et al. [35]), the information available in Tabuchi et al. [12], and Corda et al. [29] and Iranzo et al. [24] (when not available in the first) has been used in this work. Further information about the formulation and setup of the PEMFC model can be found in Refs. [22,23].

Results and discussion

The numerical results for a single straight-channel PEMFC with channel/rib width = 1.0/1.0 mm, similar to that appearing in Refs. [12,29,36] are shown and discussed in the

Table 3 – Model parameters used in the simulations (from Corda et al. [29] and Iranzo et al. [24] if not available from Tabuchi et al. [12]).

Model parameters	Units	Value
Open circuit voltage, U	V	1.0
Anode concentration exponent, γ_a	–	0.5
Cathode concentration exponent, γ_c	–	1.0
Charge transfer coefficient ($a \rightarrow a$), α_a^a	–	1.0
Charge transfer coefficient ($a \rightarrow c$), α_a^c	–	1.0
Charge transfer coefficient ($c \rightarrow a$), α_c^a	–	0.0
Charge transfer coefficient ($c \rightarrow c$), α_c^c	–	1.0
Anode reference concentration, $[A]_{ref}$	kmol/m^3	1.0
Cathode reference concentration, $[C]_{ref}$	kmol/m^3	1.0
Anode reference exchange current density, j_a^{ref}	A/m^2	5.2×10^3
Cathode reference exchange current density, j_c^{ref}	A/m^2	4.3×10^{-3}
H_2 diffusivity, $D^0_{H_2}$	m^2/s	8.0×10^{-5}
O_2 diffusivity, $D^0_{O_2}$	m^2/s	2.0×10^{-5}
H_2O diffusivity, $D^0_{H_2O}$	m^2/s	5.0×10^{-5}
Liquid blockage exponent, γ_j	–	3.5
Pore blockage saturation exponent, r_s	–	3.5
Relative permeability exponent, b	–	4.0
Phase-change rates exponent, θ	–	1.0
Mass exchange rate constant in liquid phase, γ_{ld}	–	0.5
Mass exchange rate constant in gas phase, γ_{gd}	–	2.0
Equilibrium water content at the water activity of 1, $\lambda_{a=1}$	–	9.2
Equilibrium water content at the water saturation of 1, $\lambda_{s=1}$	–	16.13

following. Because the numerical simulations can provide useful and specific information throughout a fuel cell, this work primarily focuses on the analysis of the water influence over some magnitudes of interest (say temperature, current density and O_2 concentration) under different (typical range in PEMFCs, see e.g. Ref. [4]) operating temperatures (343 K, 353 K and 363 K) at the operating pressure $P_0 = 250$ kPa.

First, it is worth mentioning that the results appearing in this section are averaged along the $yz-$ coordinate. The outcomes resulting from the $z-$ average (eq. (20)) postprocessing, are available as supplementary material. In general, following Fig. 1(*b*), these averaged quantities may be defined as

$$\bar{\phi} = \frac{1}{z}\int_z \phi \, \partial z, \tag{20}$$

$$\bar{\phi} = \frac{1}{\mathcal{S}_{yz}}\int_{\mathcal{S}} \phi \, \partial y \, \partial z, \tag{21}$$

where ϕ is any of the magnitudes of interest and $\bar{\phi}$ its averaged value, and y, z and $\mathcal{S}_{yz}$ stands for the Cartesian coordinates and the corresponding averaging plane, respectively.

The most characteristic metric defining the performance of a fuel cell is the polarization curve. For the sake of reference, the characteristic $j-V$ plot has been inserted in Fig. 2 to compare the capabilities of the PEMFC between the difference cases in study (note that, as mentioned in section 2, potentiostatic boundary conditions were selected for convenience). The three typical regions for a PEMFC are found in Fig. 2 for each of the operating temperatures. First, the activation losses separate the real cell potential from the theoretical given by Nernst equation ($j \lesssim 0.5$ A/cm^2). Next, the ohmic losses representing the linear trend in $0.5 \lesssim j \lesssim 1.5$ A/cm^2, are due to the internal resistance of the fuel cells components. Finally, the mass transfer losses, occurring at the end of the linear region ($j \gtrsim 1.5$ A/cm^2), represent the voltage drop as a consequence of the penalization of the species diffusion. This effect is mainly attributed to the water presence at very high current densities, which results in the blocking of the porous media and the flooding of the reaction surface area. It is worth mentioning that the location of each of the mentioned regions of course vary depending on the constructive and operational PEMFC characteristics. In the three cases in study the polarization curve corresponding to $T_0 = 363$ K displays a superior performance. A deeper analysis on the respective operations will be conducted in the following section.

Operating temperature $T_0 = 353$ *K*

The results corresponding to the averaged quantities eq. (20) and eq. (21) (see Fig. 1(*b*)) are displayed in this study. For the sake of brevity only the profile-like plots (these according to eq. (21)) will be discussed in the following, but contour plots (obtained through eq. (20)) are accessible from the Supplementary Material.

In general, it is shown that j is larger under-rib and decreases under-channel at high voltages ($0.75 < U < 0.65$ V), but at higher loads ($0.45 < U < 0.27$ V) the current density becomes larger at the channel/rib interface. This effect may be explained by the increment of water saturation (mostly in cathode), which decreases from the under-rib to the under-channel regions, as depicted in Fig. 3(*c*). The water appearing in the GDLs progressively reduces the porosity of such layers as the liquid fills the orifices, difficulting the diffusion process as can be seen e.g. in Fig. 3(*e*). This penalization is higher under-rib because a larger quantity of water condensates underneath due to the lower temperatures in this region (see Fig. 3(*b*)). However, at $T \geq 355$ K one can note that the increase of water saturation at $U \leq 0.45$ V is compensated by evaporation as shown by the roughly coincident curves under-rib in Fig. 3(*c*), observing an equilibrium saturation under-channel of approximately $s \simeq 0.05$. Finally, it is worth discussing the behavior of λ in Fig. 3(*d*) with respect to the temperature in Fig. 3(*b*), since the level of hydration in membrane is decisive in the PEMFC performance. Therefore, it can be seen in Fig. 3(*d*) that at $T_0 = 353$ K the water content progressively diminishes as the load increases. It means that the effect of the temperature rise with the current increase dominates over the water generated by the electrochemical reaction in the cathode

$$4H^+ + 4e^- + O_2 \rightarrow 2H_2O, \tag{22}$$

but at $U \geq 0.45$ V, the λ level seems to start being balanced by the temperature distribution through evaporation. More specifically in Fig. 3(*d*), some different trends are observed in the under-rib and under-channel regions. At small loads

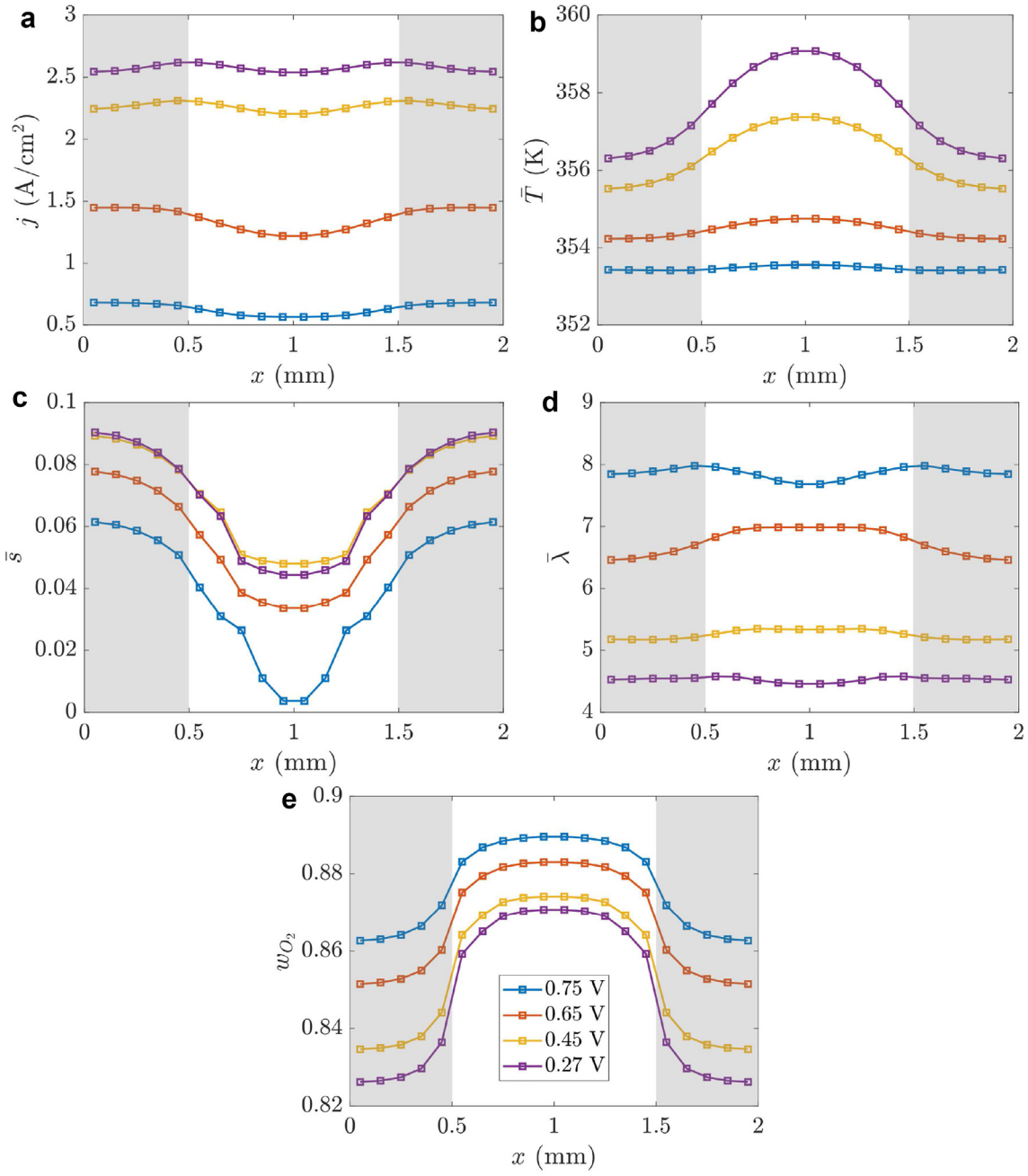

Fig. 3 – yz– weighted average of current density (*a*), temperature (*b*), and water content (*d*) across the membrane. Averaged water saturation (*c*) is reported in between GDLs and membrane. Subplot (*e*) describes the oxygen concentration average in the GDL$_c$/channel/rib interface. Shaded areas represent half-rib zones. Operating temperature is $T_0 = 353$ K.

($U = 0.75$ V) the differences between the oxygen concentration under-channel and under-rib are not very large, and the temperature under-rib is appropriate for the water condensation, λ being definitely higher under-rib. At the intermediate voltages 0.65 V $\leq U \leq$ 0.45 V, the O_2 mass fraction is sufficiently higher under-channel than under-rib as to generate a higher water content at 0.5 mm $\leq x \leq$ 1.5 mm. Contrarily, λ again decreases at the smallest voltage in the under-channel because the evaporation rate in this zone (see Fig. 3(*b*)) prevails over the water generation.

Operating temperature $T_0 = 343$ *K*

To evaluate the influence of the operating temperature on the fuel cell performance, the previous study in section 3.1 is extended to $T_0 = 343$ K, fixed the same relative humidity of the species ($RH = 90\%$) at the inlet. Similar to Fig. 3, the respective Fig. 4 will help to understand how the averaged magnitudes of interest evolve at the above-analyzed electric loads.

Like in the baseline case (Fig. 3), a profile-based composition is displayed in Fig. 4 to deeply understand the spatial

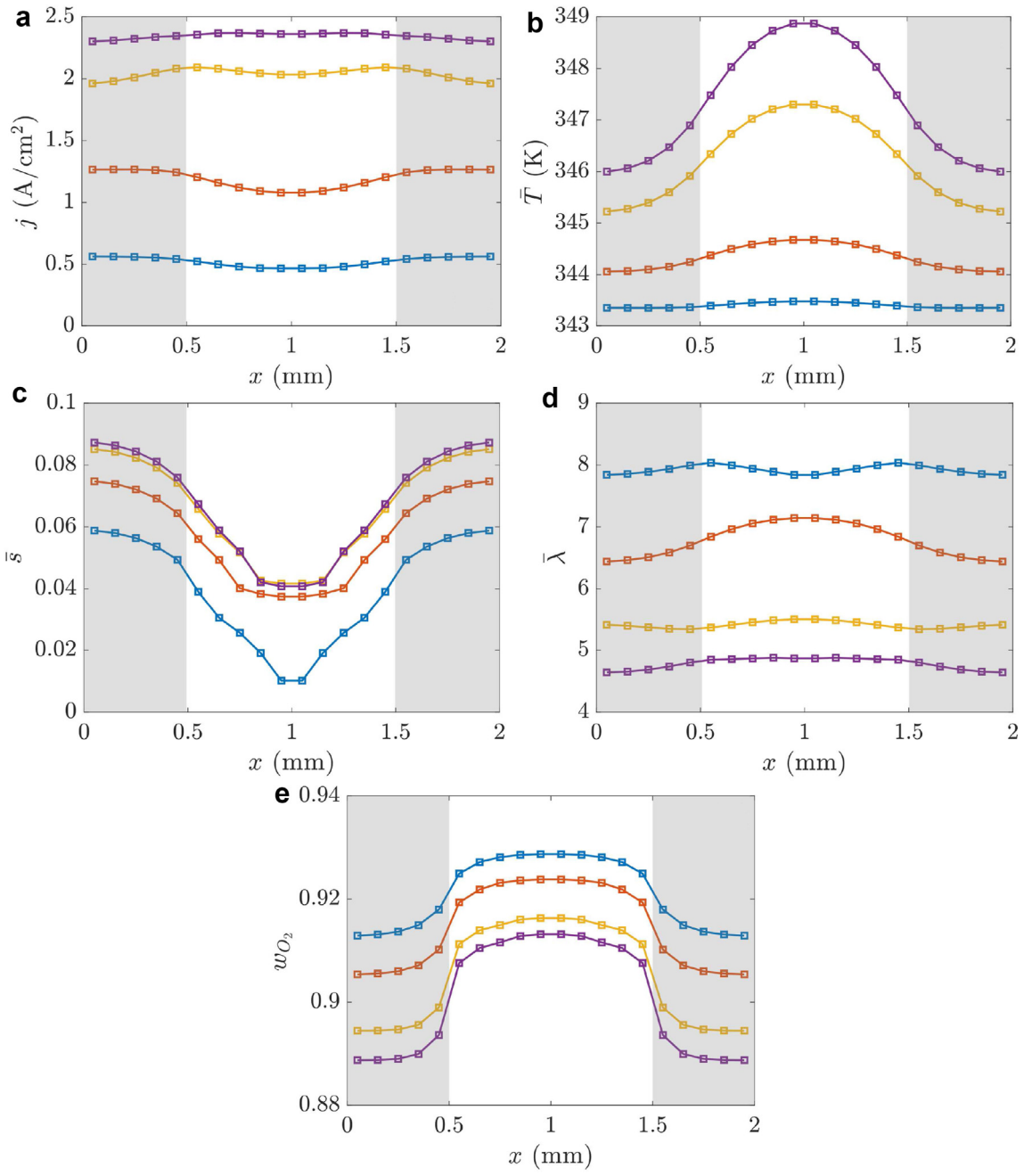

Fig. 4 – Same as in Fig. 3 but at operating temperature $T_0 = 343$ K.

evolution of j, T, s, λ and w_{O_2} when the operating temperature is decreased in 10 K. The main differences that one can observe in comparing Fig. 4(*a*) against Fig. 3(*a*) is that the outermost $j-$ curves (at $U = 0.75$, 0.27 V) show a roughly flat profile. More particularly, at the voltage $U = 0.75$ V, the current density $j \simeq 0.5$ A/cm^2 reaches comparable values to those of the corresponding operation load at $T_0 = 353$ K. However, as one increases the load above $U = 0.45$ V, the current density experiments a slight penalization with respect Fig. 3(*a*). In the limit, at $U = 0.27$ V, j is about 3% lower than the reference case.

As for the temperature in Fig. 4(*b*), it is shown that the spatial distribution perfectly matches the same trend as in Fig. 3(*b*), obtaining the maximum under-channel, of course at a smaller value. It is remarkable that the highest temperature in Fig. 4(*b*) increases a fixed quantity $\Delta T \simeq 10$ K with respect to the case in Fig. 3(*b*). To better compare the temperature variations between the different operating conditions in study, the dimensionless temperature difference is introduced as

$$\Theta = \frac{T - T_0}{T_{max} - T_0}, \tag{23}$$

where T_{max} stands for the highest temperature reached at each T_0 case. Fig. 6 displays that the temperature differences in terms of eq. (23) (for now only considering $T_0 = 343$ K vs. $T_0 = 353$ K) are quite small, with the largest discrepancies appearing under-rib, probably affected by the numerical

boundary conditions. This agreement could indicate that the temperature distribution does not depend on the operation temperature. To further analyze this effect, such comparison will be revisited in section 3.3, including the case at $T_0 = 363$ K.

Regarding the water saturation and the water content in membrane, Fig. 4(c) and (d) show small differences with respect to their counterparts in Fig. 3(c) and (d). The averaged water saturation in between GDLs at $T_0 = 343$ K seems to be comparable to that of the baseline, both under-rib and under-channel, although some differences can be hardly observed. A similar trend can be noticed in inspecting the water content in membrane at $T_0 = 343$ K. To further characterize the existing differences, a clearer assessment on λ and s can be performed by means of their volume-weighted averages in Table 4. A closer look draws that λ is slightly higher and s slightly smaller at $T_0 = 343$ K than at $T_0 = 353$ K, where a higher membrane hydration level typically results in a better performance of the PEMFC. However, one must recall that potentiostatic conditions were used in the simulations, so that the value of j separates at smaller voltages in comparing the three polarization curves in Fig. 2, with the consequent implications on the temperatures and water generation. Yet in this case, the benefits of a higher operating temperature at $T_0 = 353$ K (e.g. increased membrane proton conductivity, enhanced electrode kinetics, and improved mass transfer of the reactants [37]) surpass any water-based advantage at $T_0 = 343$ K (see section 2). This comparison will be revisited and extended with the results from the operating condition $T_0 = 363$ K. Moreover, Fig. 3 (e) shows that the O_2 concentration results higher (in the order of $\sim 10\%$) than that at $T_0 = 353$ K.

Operating temperature $T_0 = 363$ K

For the sake of completion, a higher operating temperature is finally selected at $T_0 = 363$ K, comparing the results obtained in this case with the previous in section 3.1 and section 3.2 (*RH* maintained at 90%). To conclude the comparative study, the profile-like curves across the cell width are included in Fig. 5. Fig. 5(a) shows that the current densities obtained at $T_0 = 363$ K are larger than those of the previous cases, reaching the maximum value at the under-rib region. Furthermore, one can see that the trend of j for the different voltages differs from that in Fig. 3(a) and Fig. 4(a), which can be attributed to the related water processes in Fig. 5(c) and Fig. (d). Alternatively, it is meaningful to note that the averaged temperatures in membrane in Fig. 5(b) also shows a fixed difference of $\simeq 10$ K in between consecutive operating conditions as observed when comparing $T_0 = 343$ vs. $T_0 = 353$ K. At this point, one might be interested in investigating these effects altogether in Fig. 6 through the parameter θ in Eq. (23). The results are revealing and display a clear trend relating the temperature evolution across the cell width with the electric load. A scaling law or an expression describing this effect might be useful to characterize the temperature distribution in the under-channel/under-rib regions. On the other hand, it is noticed that the income temperature of H_2 and O_2 in Fig. 5(c) is high enough for the evaporation to eliminate the water saturation under channel, practically at each operation point. Similar to Fig. 4(c) and Fig. 3(c), the under-rib zone contains the largest quantity of saturated water, which is limited at $U \leq 0.45$ V, as shown by the overlapping curves. In membrane, the cross-sectional evolution of λ in Fig. 5(d) displays a quite similar behavior as that of Fig. 3(d) except for the highest load, where the temperatures at $T_0 = 363$ K contribute to a larger water removal by evaporation under-channel, resulting in the smallest value of λ ($\bar{\lambda} < 4$) throughout the entire study.

The water influence is compared in Table 4 including the three operating temperatures in ascendant order. The comparison shows that both the water content and saturation are comparable at high voltages ($0.75\text{ V} \leq U \leq 0.65$ V) because the current density at these points is small (the differences in Fig. 2 are small, practically coinciding all of them in j for each U) and the water generation balances evaporation for each T_0, approximately at the same rate. Alternatively, at lower potentials ($U \leq 0.45$ V) one may want to conduct such comparison at the same current densities to separately evaluate the existing relation between the water generation and saturation, and the operating temperature. Thus, Table 5 displays the values of Table 4 at the coincident j points assigned by the baseline case.

The values of λ and s in table 5 at low current densities ($0.62 \leq j \leq 1.34$ A/cm^2) are assumed to be comparable to those in table 4 (see Fig. 2). At higher loads ($j \geq 2.25$ A/cm^2), in contrast, the differences are more evident, although the trend is the same as that obtained by comparing potentiostatic conditions in Table 4 and i.e. the water content in membrane is smaller at 343 K than at 353 K. As one initially might think, the lower the temperature is, the less the evaporation and the larger the water quantity in membrane. However, there are some other processes affecting this behavior that will be explained below.

The water production rate is determined theoretically by means of Faraday's law, i.e.

$$\dot{m}_{H_2O,\,gen} = \frac{I}{2F} M_{H_2O}. \tag{24}$$

which provides the overall water generation occurring in the entire PEMFC. In membrane, nevertheless, the water transport is a complex process involving some other

Table 4 – Volume-weighted average of the water content in membrane λ, water saturation in the cathode GDL s_c, and current density magnitude j (A/cm^2) on terminal plates, at the different operating conditions considered in this work.

U (V)	$T_0 = 343$ K			$T_0 = 353$ K			$T_0 = 363$ K		
	$\bar{\lambda}$	$\bar{s}_c$	$\bar{j}$	$\bar{\lambda}$	$\bar{s}_c$	$\bar{j}$	$\bar{\lambda}$	$\bar{s}_c$	$\bar{j}$
0.75	7.922	0.088	0.524	7.862	0.089	0.615	7.803	0.082	0.715
0.65	6.782	0.133	1.654	6.748	0.134	1.833	6.688	0.128	2.037
0.45	5.407	0.148	2.031	5.252	0.158	2.182	5.008	0.138	2.452
0.27	4.784	0.151	2.334	4.530	0.156	2.438	4.155	0.133	2.790

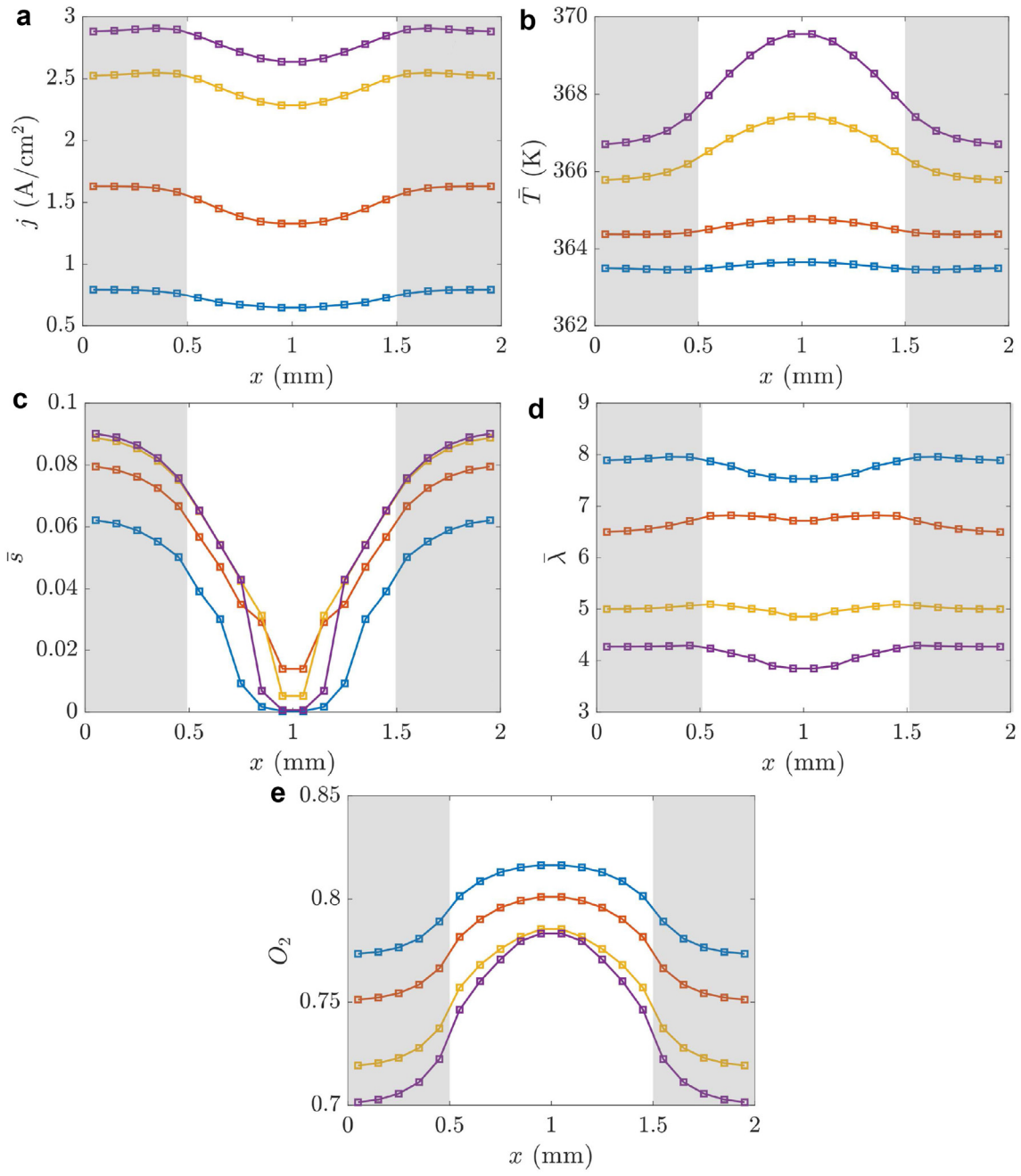

Fig. 5 – Same as in Fig. 3 but at operating temperature $T_0 = 363$ K.

mechanisms such as back diffusion and EOD (electro-osmotic drag), both depending on temperature. These effects were also noticed by Falcão et al. [38], who discovered that for a given current density the water content in membrane increased with temperature. They also found that the water diffusivity grows with the operating temperature when ranging in j.

Therefore, according to e.g. Park and Caton [39], the water generation rate in membrane can be quantified through the water flux obtained from the EOD

$$\dot{m}_{H_2O,\,drag} = n_d \frac{I}{F} M_{H_2O}, \tag{25}$$

and through the water back-diffusion flux

$$\dot{m}_{H_2O,\,back-diff} = \frac{\rho}{EW} D_w \frac{d\lambda}{dy}, \tag{26}$$

with $d\lambda/dy$ the spatial variation of the water content perpendicular to the membrane (see Fig. 1 for the system of reference). The water generation rate in membrane can be eventually calculated as the sum of eq. (25) and eq. (26). Alternatively, n_d and D_w were experimentally determined in Ref. [39]. Here, numerical simulations allow to compute their volume-weighted averages at the current densities in Table 4, $j = 2.25$ and 2.5 A/cm^2. As reported in Table 6, one can observe that according to Ref. [38] the value of both n_d and D_w increases with temperature, which explains the higher water content at

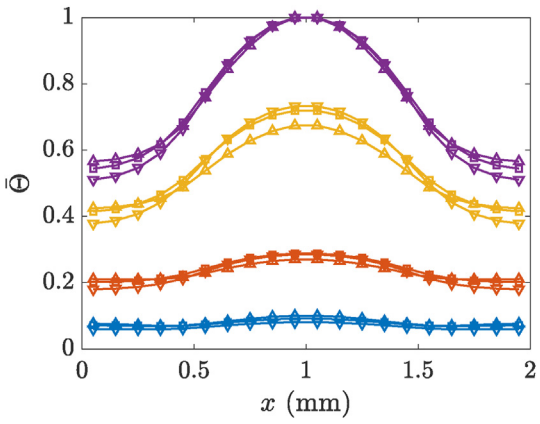

Fig. 6 – Same as in Fig. 3 but for the parameter Θ at the operating temperatures: □ $T_0 = 353$ K, ▽ $T_0 = 343$ K, and △ $T_0 = 363$ K.

Table 5 – Same as in table 4 but using galvanostatic conditions at the given current densities. The missing data at $T_0 = 343$ K indicates that the PEMFC cannot reach these operation conditions (see polarization curve in Fig. 2).

j (A/cm^2)	$T_0 = 343$ K		$T_0 = 353$ K		$T_0 = 363$ K	
	$\bar{\lambda}$	$\bar{s}_c$	$\bar{\lambda}$	$\bar{s}_c$	$\bar{\lambda}$	$\bar{s}_c$
2.25	4.961	0.052	5.252	0.158	5.384	0.136
2.57	–	–	4.530	0.156	4.783	0.045

Table 6 – Volume-weighted average of the EOD and water diffusion coefficients in the membrane at the different operating temperatures in study and $j = 2.25$ and 2.5 A/cm^2.

	$j = 2.25$ A/cm^2			$j = 2.57$ A/cm^2		
T_0	343 K	353 K	363 K	343 K	353 K	363 K
$\bar{n}_d$	0.963	1.045	1.050	–	0.870	0.920
$\bar{D}_w(\times 10^{-9})$	9.100	9.550	9.820	–	8.364	8.980

higher temperatures when evaporation does not dominate the membrane hydration.

Finally, as for the water saturation in table 4, it can be deduced from the previous results that s is tightly related to λ. At $T_0 = 343$ K and 353 K the water saturation level agrees with the water content in membrane. However, even though at $T_0 = 363$ K the λ magnitude still increases, the quantity of water saturation decreases with respect to these at $T_0 = 353$ K because evaporation at $T_0 = 363$ K starts playing a dominant role, which may result in a poorer PEMFC performance at operating temperatures above $T_0 = 363$ K. A more compact way to correlate the interaction taking place between different water-related magnitudes will be discussed in the following.

General remarks

To conclude the former analysis, Fig. 7 provides a more compact way to summarize the most relevant findings of this study, correlating the overall relationship of the temperature and current density against the membrane water content (*a*) and the water saturation in porous media (*b*), for the different operating temperatures (T_0) and potential conditions (U). It can be observed in Fig. 7(*a*) (and already discussed in section 3.1–section 3.3), that the averaged water quantity in membrane increases with T_0 as with the current density, mainly as a consequence of the electrochemical reaction. The same pattern is clearly observed in Fig. 7(*b*) for the water saturation. Therefore, these scatter plots permit to explore the variations of T and j, simultaneously.

For instance, it can be found that at high voltages ($0.75 < U < 0.45$ V), the PEMFC temperature remains practically constant throughout the fuel cell. However, at $U \leq 0.45$ V ($j > 1$ A/cm^2), it is shown that the spatial variations of j are larger than those for the case at the maximum potential ($U = 0.75$ V), barely exhibiting variation. In particular, for $U \leq 0.45$ V, the gradients of T are accompanied by larger gradients of j.

In terms of λ (see Fig. 7(*a*)), however, the largest variations and smallest magnitudes are in general distinguished at high temperatures (occurring of course at higher T_0). This feature might be explained through a competition between water generation and evaporation. At high temperatures (say $T > 365$ K) and low/intermediate current densities ($0.5 < j < 2$ A/cm^2), the heat originated inside the PEMFC starts compensating the water generation in membrane via evaporation. Because the exothermic reaction takes place under-channel, high local temperatures appear in this zone, resulting in larger temperature gradients and therefore in larger λ

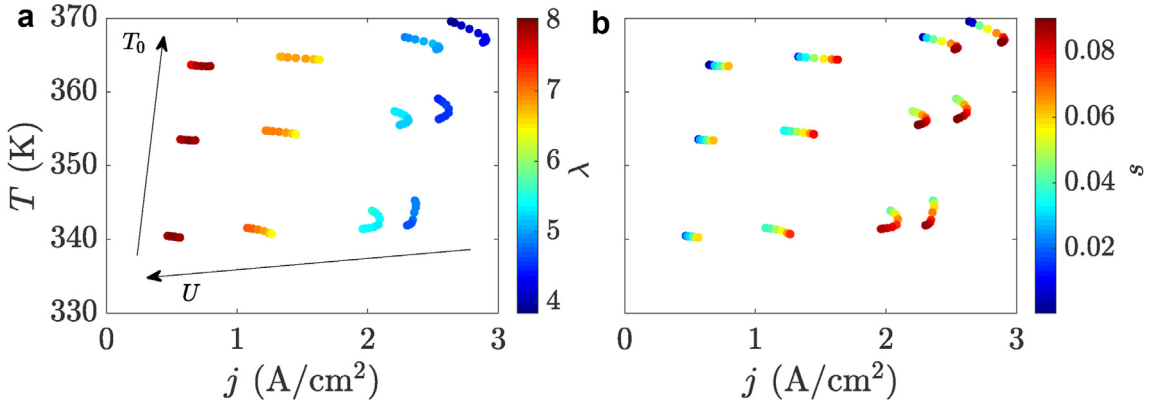

Fig. 7 – Overall relation of T and j vs. λ (*a*) and s (*b*) for the different operating temperatures and potentiostatic conditions. Increasing T_0 and U values in (*b*) follow the same directions as these in (*a*).

variations. This effect is even more noticeable at larger current densities, where the highest temperature gradients appear (see the curvy-like dot sets).

Alternatively, because the water in porous media in Fig. 7(*b*) typically condensates under-ribs and evaporates under-channel due to the local temperature distributions (see Figs. 3–5(*b*) and (*c*)), the largest gradients of *s* are clearly visible that occur at large current densities and at high operating temperatures. The highest value of *s* is of course found at large current densities because more oxygen is required to overcome the given potential.

Finally, it can be highlighted that the correlation of the water quantities λ and *s* with respect to some other variables by using colored scatter plots is a useful method to explore and understand existing relations and scales quantifying these processes.

Conclusions

The performance of a single straight-channel PEMFC was studied numerically with a suitably validated model. Three different operating temperatures are explored: 343 K, 353 K and 363 K; analyzing the interactions that take place between current density, temperature, water saturation in GDLs, water content in membrane and oxygen concentration in the cathode. The relative humidity of species at the inlet was fixed at $RH = 90\%$ for both the H_2 and O_2 inlet streams in order to investigate the sensitivity on the operating temperature. The operating pressure was maintained at 250 kPa for all the cases.

Given the aforementioned conditions, steady-state numerical simulations were conducted for a fixed range of voltages of interest, namely $U = 0.75, 0.65, 0.45, 0.27$ V, for each of the operating temperatures. Some additional cases were run to compare results in terms of a given density current. Although several contour plots compositions (see Supplementary Material) helped to understand the spatial evolution of the variables and their interactions, profile-like (i.e. weighted averaged magnitude vs. cell width coordinate) and colored scatter charts were essential to establish under-channel and under-rib conclusions. Moreover, because many physical processes are coupled during the PEMFC performance, the latter kind of plots offer a compact way to correlate magnitudes.

In general terms, the resulting polarization curves reveal a performance of the PEMFC that increases with the value of T_0 in study, reaching the largest current densities at 363 K. The benefits of a high operating temperature are unquestionable under these operation conditions because it has been shown that temperature improves the electrochemical kinetics, as well as the electro-osmotic drag and water diffusivity. The main findings of this work can be summarized as follows.

- At the studied temperatures and *RH*, evaporation effects are not so important as to decrease the PEMFC performance, although a decrease on the water saturation and membrane hydration levels starts being visible at 363 K. Probably, a further increase of the operating temperature beyond 363 K might lead to a poorer performance of the PEMFC.
- It is significant the agreement obtained between the temperature profile plots in dimensionless form for the three different operating temperatures considered in this work. Future efforts on the characterization of these curves via analytical expressions or scaling laws might be of practical interest for the PEMFC design. Such an analysis has not been previously addressed in a straight-channel PEMFC and might be useful e.g. for the prediction of the cross-sectional averaged temperatures under different operating conditions.
- The oxygen concentration levels are mainly affected by the molar fraction of the species at the inlet in order to maintain $RH = 90\%$ constant when varying T_0. The distributions of the O_2 consumption are very similar between the three operating temperatures, with the highest values found under-channel and the lowest under-rib, as expected. It has been shown that the oxygen concentration diminishes of course with the load increase.

To conclude, a valuable number of numerical results has been reported in a single straight-channel geometry with the aim to understand the interaction between the most significantly variables in a PEMFC influencing its performance, in order to improve the operating conditions or designs. For extension of the work, only cross-sectional averages are disclosed, remaining open similar analysis over the longitudinal coordinates. On the other hand, even though an exhaustive sensitivity study was addressed, it has been demonstrated that the isolation of a single variable from the rest in a PEMFC is not always possible given the diverse nature and coupling of the processes involved.

Declaration of competing interest

The authors declare that they have no known competing financial interests or personal relationships that could have appeared to influence the work reported in this paper.

Acknowledgments

This publication has been possible thanks to the following grants: Grant PY20 RE 315 026 AICIA funded by S.G. de Universidades, Investigación y Tecnología, PAIDI 2020 program 316 by Junta de Andalucía, co-funded with ERDF funds. Grant PID2019–104441RBI00 funded by 317 MCIN/AEI/10.13039/501100011033, co-funded with ERDF funds.

Appendix A. Supplementary data

Supplementary data to this article can be found online at https://doi.org/10.1016/j.ijhydene.2022.12.281.

REFERENCES

[1] Olabi A, Wilberforce T, Abdelkareem MA. Fuel cell application in the automotive industry and future perspective. Energy 2021;214:118955.
[2] Nazir H, Louis C, Jose S, Prakash J, Muthuswamy N, Buan ME, Flox C, Chavan S, Shi X, Kauranen P, et al. Is the H2 economy realizable in the foreseeable future? Part I: H2 production methods. Int J Hydrogen Energy 2020;45:13777–88.
[3] Zuo W, Zhao H, Jiaqiang E, Li Q, Li D, Yang D, Zhao Y. Effects of injection strategies on thermal performance of a novel micro planar combustor fueled by hydrogen. Int J Hydrogen Energy 2022;47:9018–29.
[4] Barbir F. PEM fuel cells: theory and practice. Academic press; 2012.
[5] Li H, Tang Y, Wang Z, Shi Z, Wu S, Song D, Zhang J, Fatih K, Zhang J, Wang H, et al. A review of water flooding issues in the proton exchange membrane fuel cell. J Power Sources 2008;178:103–17.
[6] Ji M, Wei Z. A review of water management in polymer electrolyte membrane fuel cells. Energies 2009;2:1057–106.
[7] Ijaodola O, El-Hassan Z, Ogungbemi E, Khatib F, Wilberforce T, Thompson J, Olabi A. Energy efficiency improvements by investigating the water flooding management on proton exchange membrane fuel cell (PEMFC). Energy 2019;179:246–67.
[8] Pourrahmani H, Yavarinasab A, Siavashi M, Matian M, et al. A review on the proton exchange membrane fuel cells (PEMFCs) water/thermal management: from theory to the current challenges and real-time fault diagnosis methods. Energy Rev 2022:100002.
[9] Yang Z, Du Q, Jia Z, Yang C, Jiao K. Effects of operating conditions on water and heat management by a transient multi-dimensional PEMFC system model. Energy 2019;183:462–76.
[10] Iranzo A, Arredondo C, Kannan A, Rosa F. Biomimetic flow fields for proton exchange membrane fuel cells: a review of design trends. Energy 2020;190:116435.
[11] Suárez C, Iranzo A, Toharias B, Rosa F. Experimental and numerical Investigation on the design of a bioinspired PEM fuel cell. Energy 2022;257:124799.
[12] Tabuchi Y, Shiomi T, Aoki O, Kubo N, Shinohara K. Effects of heat and water transport on the performance of polymer electrolyte membrane fuel cell under high current density operation. Electrochim Acta 2010;56:352–60.
[13] Iranzo A, Gregorio JM, Boillat P, Rosa F. Bipolar plate research using Computational Fluid Dynamics and neutron radiography for proton exchange membrane fuel cells. Int J Hydrogen Energy 2020;45:12432–42.
[14] Yoshimune W, Kato S, Inagaki M, Yamaguchi S. A simple method to measure through-plane effective gas diffusivity of a gas diffusion layer for polymer electrolyte fuel cells. Int J Heat Mass Tran 2022;191:122887.
[15] Yuan W, Li J, Xia Z, Chen S, Zhang X, Wang Z, Sun H. Study of water transport mechanism based on the single straight channel of proton exchange membrane fuel cell. AIP Adv 2020;10:105206.
[16] Wang Y, Wang X, Qin Y, Zhang L, Wang Y. Three-dimensional numerical study of a cathode gas diffusion layer with a through/in plane synergetic gradient porosity distribution for PEM fuel cells. Int J Heat Mass Tran 2022;188:122661.
[17] Martín-Alcántara A, González-Morán L, Pino J, Guerra J, Iranzo A. Effect of the gas diffusion layer design on the water management and cell performance of a PEM fuel cell. Processes 2022;10:1395.
[18] Hamrang A, Abdollahzadeh M, Kermani M, Rahgoshay S. Numerical simulation of the PEM fuel cell performance enhancement by various blockage arrangement of the cathode serpentine gas flow channel outlets/inlets. Int J Heat Mass Tran 2022;186:122475.
[19] Su A, Ferng Y, Shih J. CFD investigating the effects of different operating conditions on the performance and the characteristics of a high-temperature PEMFC. Energy 2010;35:16–27.
[20] Rostami L, Haghshenasfard M, Sadeghi M, Zhiani M. A 3D CFD model of novel flow channel designs based on the serpentine and the parallel design for performance enhancement of PEMFC. Energy 2022;258:124726.
[21] Zhang Y, He S, Jiang X, Xiong M, Ye Y, Yang X. Three-dimensional multi-phase simulation of different flow fields with cooling channel in proton exchange membrane fuel cell. Int J Hydrogen Energy 2022;47:37929–44.
[22] Ansys fluent theory guide. Ansys Inc., U.S.A.; 2022. p. 845–80.
[23] Ansys fluent user's guide. Ansys Inc., U.S.A.; 2022. p. 3099–190.
[24] Iranzo A, Munoz M, Rosa F, Pino J. Numerical model for the performance prediction of a PEM fuel cell. Model results and experimental validation. Int J Hydrogen Energy 2010;35:11533–50.
[25] Zhang G, Fan L, Sun J, Jiao K. A 3D model of PEMFC considering detailed multiphase flow and anisotropic transport properties. Int J Heat Mass Tran 2017;115:714–24.
[26] Awan A, Saleem M, Basit A. Simulation of proton exchange membrane fuel cell by using ANSYS fluent. In: IOP conference series: materials science and engineering, vol. 414; 2018, 012045. IOP Publishing.
[27] Iranzo A, Boillat P. CFD simulation of the transient gas transport in a PEM fuel cell cathode during AC impedance testing considering liquid water effects. Energy 2018;158:449–57.
[28] Zhou Z, Qiu D, Peng L, Lai X. Channel/rib patterns optimization of a proton exchange membrane fuel cell by combining down-the-channel performance model and genetic algorithm. Int J Heat Mass Tran 2022;183:122235.
[29] Corda G, Fontanesi S, d'Adamo A. Methodology for PEMFC CFD simulation including the effect of porous parts compression. Int J Hydrogen Energy 2022;47:14658–73.
[30] Li W, Zhang Q, Wang C, Yan X, Shen S, Xia G, Zhu F, Zhang J. Experimental and numerical analysis of a three-dimensional flow field for PEMFCs. Appl Energy 2017;195:278–88.
[31] Wu P-K, Tseng L-K, Faeth GM. Primary breakup in gas/liquid mixing layers for turbulent liquids. Atomization Sprays 1992;2.
[32] Scholz H. Modellierung und Untersuchung des Wärme-und Stofftransports und von Flutungsphänomenen in Niedertemperatur-PEM-Brennstoffzellen, Diss. RWTH Aachen; 2015.
[33] Um S, Wang C-Y, Chen K. Computational fluid dynamics modeling of proton exchange membrane fuel cells. J Electrochem Soc 2000;147:4485.
[34] Wu H, Li X, Berg P. On the modeling of water transport in polymer electrolyte membrane fuel cells. Electrochim Acta 2009;54:6913–27.
[35] Rezk H, Olabi A, Ferahtia S, Sayed ET. Accurate parameter estimation methodology applied to model proton exchange membrane fuel cell. Energy 2022;255:124454.
[36] D'Adamo A, Riccardi M, Locci C, Romagnoli M, Fontanesi S. Numerical simulation of a high current density PEM fuel cell, technical report. SAE Technical Paper; 2020.
[37] Zhang J, Wu J, Zhang H, Zhang J. PEM fuel cell testing and diagnosis. Newnes; 2013.
[38] Falcão D, Pinho C, Pinto A. Water management in PEMFC: 1-D model simulations. Ciência & Tecnologia dos Materiais 2016;28:81–7.
[39] Park YH, Caton JA. An experimental investigation of electro-osmotic drag coefficients in a polymer electrolyte membrane fuel cell. Int J Hydrogen Energy 2008;33:7513–20.